

Pinning induced motion and internal flow in neighbouring evaporating multi-component drops

Pim J. Dekker^{1†}, Marjolein N. van der Linden²¹ and Detlef Lohse^{13‡}

¹Physics of Fluids group, Department of Science and Technology, Max Planck Center for Complex Fluid Dynamics and J. M. Burgers Centre for Fluid Dynamics, University of Twente, P.O. Box 217, 7500 AE Enschede, The Netherlands

²Canon Production Printing Netherlands B.V., P.O. Box 101, 5900 MA Venlo, The Netherlands

³Max Planck Institute for Dynamics and Self-Organization, Am Fassberg 17, 37077 Göttingen, Germany

(Received xx; revised xx; accepted xx)

The evaporation of multi-component sessile droplets is key in many physicochemical applications such as inkjet printing, spray cooling, and micro-fabrication. Past fundamental research has primarily concentrated on single drops, though in applications they are rarely isolated. Here, we experimentally explore the effect of neighbouring drops on the evaporation process, employing direct imaging, confocal microscopy, and PTV. Remarkably, the centres of the drops move away from each other rather than towards each other, as we would expect due to the shielding effect at the side of the neighbouring drop and the resulting reduced evaporation on that side. We find that pinning-induced motion mediated by suspended particles in the droplets is the cause of this counter-intuitive behaviour. Finally, the azimuthal dependence of the radial velocity in the drop is compared to the evaporative flux and a perfect agreement is found.

Key words:

1. Introduction

The evaporation of sessile droplets has received considerable attention, both because of fundamental scientific interest and because of its importance to many technological and biological applications, such as inkjet printing (Hoath 2016; Wijshoff 2018; Lohse 2022), spray cooling (Cheng *et al.* 2016), nanofabrication (Brinker *et al.* 1999), pesticide spraying (Yu *et al.* 2009; Gimenes *et al.* 2013), and diagnostics (Zang *et al.* 2019). The interest in evaporating drops has taken a leap since the description of the “coffee stain effect” by Deegan *et al.* (1997). Since then, major progress has been made in the understanding of evaporating drops (Zang *et al.* 2019; Lohse 2022; Gelderblom *et al.* 2022; Wang *et al.* 2022; Wilson & D’Ambrosio 2023).

It is understood that the drop lifetime depends on the behaviour of the contact line (Nguyen *et al.* 2012; Stauber *et al.* 2014, 2015) and on evaporative cooling (Dunn *et al.* 2009). The flow in isolated evaporating drops has also been extensively studied (Deegan

† Email address for correspondence: p.j.dekker@utwente.nl

‡ Email address for correspondence: d.lohse@utwente.nl

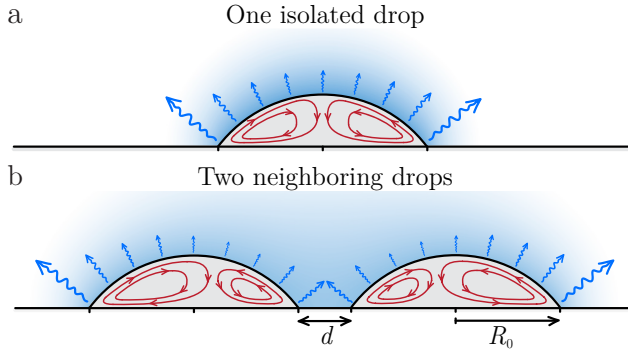


FIGURE 1. Sketch of the evaporating drop. (a) Isolated drop. The arrows in the drop indicate the Marangoni flow in the drop. The arrows on the drop surface indicate the evaporative mass flux. The colour gradient indicates the increased relative humidity around the drop. (b) neighbouring drops. Two identical drops with radius R_0 that are placed at a distance d apart. In the central region between the drops, the evaporation is reduced due to the shielding effect.

et al. 2000; Larson 2014; Edwards *et al.* 2018; Diddens *et al.* 2021; Gelderblom *et al.* 2022). For small drops, i.e. smaller than the capillary length, $l_c = (\gamma/\rho g)^{1/2} \gg R_0$, the drop shape is a spherical cap. In an evaporating drop, a replenishing (capillary) flow must develop for a drop to keep this shape.

Additionally, there can be surface tension gradients on the drop surface which lead to a Marangoni flow. These surface tension gradients can arise due to evaporative cooling, due to compositional gradients of the drop constituents because of selective evaporation, or because of the presence of surfactants at the interface. Typically, the thermal Marangoni flow due to evaporative cooling is much weaker as compared to the solutal Marangoni flow (Gelderblom *et al.* 2022). When the Marangoni flow (either solutal or thermal) in the drop is sufficiently large, the apparent contact angle of the drop can increase, which is known as Marangoni contraction (Karpitschka *et al.* 2017; Shiri *et al.* 2021; Kant *et al.* 2024). In the extreme case, the shape can even deviate from a spherical cap shape (Pahlavan *et al.* 2021).

Recently, due to the relevance for applications, more attention has also been given to the evaporation of multiple neighbouring droplets. When an isolated drop of water evaporates, the surrounding water vapour concentration is increased. When the second drop is close enough, the water vapour concentration will be further enhanced. This locally increases the ambient relative humidity that each drop experiences compared to the case of an isolated drop, which in turn increases the lifetime of neighbouring drops (Fabrikant 1985; Laghezza *et al.* 2016; Hatte *et al.* 2019; Khilifi *et al.* 2019; Chong *et al.* 2020; Schofield *et al.* 2020; Edwards *et al.* 2021; Masoud *et al.* 2021). Additionally, the evaporative flux $J = J(r, \theta)$ on the surface of each drop is no longer axisymmetric but is now a function of the azimuthal angle (Wray *et al.* 2020). For example, for two drops close to each other, the side of the drop that is facing the neighbouring drop is shielded more than the part of a drop that faces away from the neighbouring drop. This means that the evaporative flux in the region between the drops is reduced by the presence of the other drop, as illustrated in figure 1 (b).

The asymmetric flux also affects the solute deposition around the drop. The amount of solute deposited will be smaller in regions where the flux is reduced the most and is larger where the flux is reduced the least (Wray *et al.* 2021). Additionally, the solutal Marangoni flow will also become asymmetric. When the two drops also experience Marangoni contraction, the drops will start to move since the Marangoni contraction

is reduced on the side of the other drop. Depending on the composition, the drops can attract, repel, and even chase each other (Cira *et al.* 2015).

Despite the commonality of evaporating neighbouring multi-component droplets in nature and technology, little is known about the flows inside the drops and how they affect each other. Both the internal flow and the pinning-induced motion of neighbouring drops are crucial for many applications where either the position of the drop or the deposition of solute is important. Here, we will focus on binary drops of water with 1,2-hexanediol. We investigate the flow in these evaporating multi-component drops next to each other using confocal microscopy for PTV and synchronized side view shadowgraphy in a humidity-controlled chamber. Hexanediol is non-volatile and has a lower surface tension than water, resulting in solutal Marangoni flow. We show that this flow is indeed asymmetric as expected, and we find perfect agreement with the local evaporative flux. Counter-intuitively, as the drops evaporate, we observe that the drops move apart.

2. Experimental procedure

The experiments were performed in a humidity and temperature-controlled chamber at $\text{RH} = (47 \pm 5)\%$ and $T = (23.8 \pm 0.3)^\circ\text{C}$. During the measurements the airflow was disabled. The chamber volume ≈ 0.75 l was sufficiently large to ensure diffusion-limited evaporation. The binary mixtures consisted of 10 wt% 1,2-hexanediol (Sigma-Aldrich, 98% pure) which is non-volatile, and 90 wt% water (“Milli-Q”, resistivity 18 M Ω cm) which is volatile. The drops were manually deposited using a syringe (Hamilton, model 7001) on a glass slide coated with transparent hydrophobic octadecyltrichlorosilane (OTS). The time between the depositing of the first drop and the second drop (10 s) was much shorter than the total lifetime of the drops (4.5 minutes). The volume of each drop was 0.15 μl , which is the largest drop size that fits completely in the field of view of the confocal microscope.

The drop was imaged from the side using a camera (Nikon D850) and a long-distance microscope at 7x magnification (Navitar 12x Zoom), and simultaneously from below with a confocal microscope (Nikon A1R). By adding a small amount of polystyrene fluorescent particles (microParticles GmbH, concentration = $3.8 \cdot 10^{-3}$ vol%, diameter = 1.14 μm , $\lambda_{\text{absorption}} = 530$ nm, $\lambda_{\text{emission}} = 607$ nm) and tracking these particles with a particle tracking velocimetry (PTV) algorithm we were able to measure the flow in the drop. Since the confocal microscope had a very narrow depth of field, we were only able to detect particles that were very close to the substrate (≈ 18 μm). The confocal microscope is able to provide a bright field view of the drop (Transmission Detection) at the same time as the fluorescent image. More details of the experimental setup and data analysis are provided in the SI.

3. Contact line behaviour

Figure 2 (a,b,c) shows snapshots of the side view at different times of two evaporating drops. Figure 2 (f) shows the bottom view of the right drop in figure 2 (c). Figure 2 (a) shows the drops just after they have been deposited on the substrate. The initial drop contact radius is $R_0 = 0.53$ mm and the distance between the drop edges is $d/R_0 = 1.7$. As a visual guide, the position of the contact line has been marked by a dashed line, which extends into the next panel. The position of the contact line is also marked in the bottom view with a dashed line in figure 2 (f). For the first 180 s after the drop deposit, the drop evaporates in a constant contact angle mode. The contact line of each drop

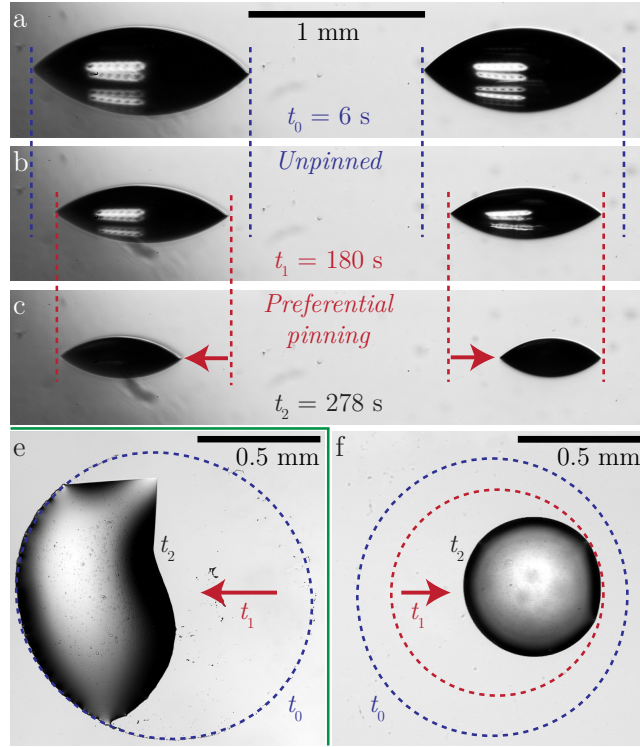


FIGURE 2. (a,b,c) Show three snapshots of the side view of two drops evaporating. Figure (a), taken at $t_1 = 6$ s, shows how the two drops are deposited. The position of the contact line is marked with the dashed line and is extended into the next snapshot for reference. For the first 180 s of the evaporation, the drops are unpinned. In figure (b), taken at $t_1 = 180$ s, both drops get pinned only on the far side w.r.t. the other drop. Because of the partial pinning of the drops they start to move apart. In figure (c), taken at $t_2 = 278$ s, the water has stopped evaporating. Figure (f) shows the bottom view of the right drop shown in (a,b,c). The dashed lines correspond to t_0 , the original size of the drop, and t_1 , the moment the drop becomes partially pinned. The left drop looks correspondingly but moves to the other side. Figure (e) Shows a different case where the drop was pinned from the start but unpinned at some time on one side only. The other drop was on the right of the drop in (e).

moves the same distance inwards on all sides. Up to that time, the centres of both drops remain in the same place.

However, after some more time, we see that the centres of the drops move *away* from each other. Figure 2 (b) shows the moment when the drops start to move away from each other. Again the position of the contact line is marked with a dashed line. Figure 2 (c) shows the residue of the non-volatile 1,2-hexanediol when the evaporation of water in the drop has stopped. Going from panel (b) to (c), we see that the contact line facing away from the other drop has stayed in place, while the contact line facing toward the other drop has retracted. During the whole evaporation, the contact angle of both drops remained the same.

The movement of the drops *away* from each other is very surprising: the direction is opposite to what would be predicted based on the shielding effect. Since the evaporation is highest in regions facing away from the other drop, one would expect the contact line to recede more quickly in those regions, and consequently move towards the other drop. We will now explore possible explanations for this behaviour.

Water/1,2-hexanediol mixtures are known to show Marangoni contraction ([Hack et al. 2021](#)). Since the contact line will contract more strongly in the region facing away from the other drop, we would expect the drops to move toward each other. Therefore, Marangoni

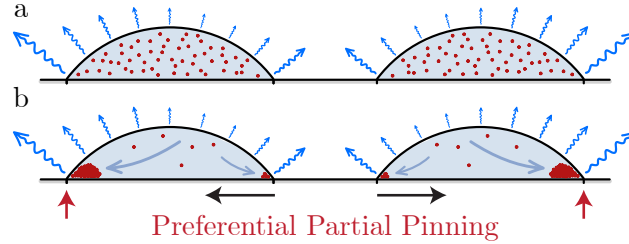


FIGURE 3. Schematic of the preferential partial pinning effect. (a) Initially, the particles are distributed homogeneously throughout the drop. Owing to the shielding effect, evaporation is suppressed in the area between the drops. (b) This results in most particles agglomerating at the side opposite the other drop due to the higher flux there. This will make it more likely that the drop pins on that side only because of the larger number of particles there.

contraction cannot be the origin of the drop movement. Furthermore, during the first part of the evaporation process ($t_0 \rightarrow t_1$) we observe no significant displacement of the drops, indicating that the Marangoni contraction in this case is not sufficiently strong to have an effect. For Marangoni contraction to have an effect, the Marangoni flow must be very strong. This requires both a very large surface tension gradient as well as a very low contact angle, which is not the case here.

Ruling out capillary flow and Marangoni contraction, we are left with the hypothesis that the motion of the drops is strongly influenced by particles present in the drop. Due to the strong evaporation at the rim of the drop, particles accumulate at the contact line. Despite the Marangoni flow mixing the particles throughout the drop (Thayyil Raju *et al.* 2022), more particles will deposit and accumulate at the contact line where the evaporative flux is the largest (Wray *et al.* 2021). This results in a large concentration of particles in the region facing away from the other drop, increasing the likelihood of the drop pinning there, as is illustrated in figure 3.

The contact line behaviour in drops is typically very stochastic. Many factors influence the pinning behaviour of a drop, such as the substrate wettability and roughness (Bor-mashenko *et al.* 2011; Mampallil & Eral 2018), local drop composition at the contact line, the number and type of particles at the contact line, and the ambient temperature and relative humidity. This makes it very difficult to predict when a drop will pin or not.

In our experiments, we also experience some variability regarding the contact line behaviour. For example, figure 2 (e) shows a different case of pinning-induced motion (the left drop is shown, with the other drop being on the right). Here the drop was pinned from the start and evaporated in constant contact radius mode. This was the case until the moment that the drop suddenly unpinned on one side and moved away from the other drop. This is different for the drops shown in (a,b,c), which were evaporating in CCA mode and got pinned on one side during the evaporation. In both cases, figure 2 (e) and (f), the result is that the drops move apart. Additionally, sometimes the drop would not exhibit any pinning-induced motion and evaporate in CCR or CCA during its entire lifetime. In all cases in which the drop moved, they always moved apart.

4. Internal flow

To further elucidate the interplay between pinning, evaporation, particle deposition, and Marangoni flow, we have imaged the flow in the drops with PTV (Particle Tracking Velocimetry). Figure 4 (a) and (b) show the trajectories of the particles close to the substrate during the first 15% of the total evaporation lifetime. By limiting the analysis to

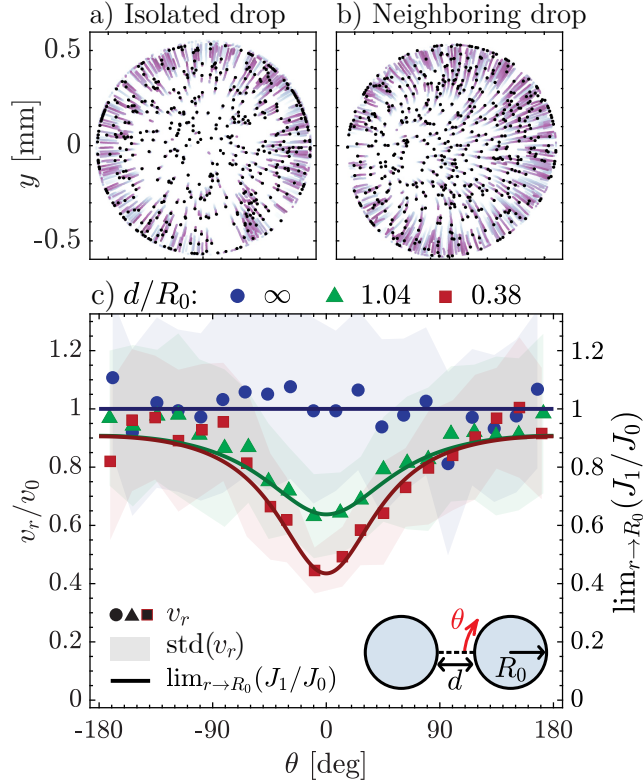


FIGURE 4. (a,b) Show the traces of particles in the drop close to ($\approx 18 \mu\text{m}$) the substrate for the first 15% of the total evaporation time. (a) Is for an isolated drop. (b) is for a neighbouring drop with $d/R_0 = 0.38$. (c) The azimuthal dependence of the averaged radial velocity in the drop close to the rim is shown for three drop separations: $d/R_0 = \{\infty, 1.04, 0.38\}$ with the symbols $\{\bullet, \blacktriangle, \blacksquare\}$, respectively. The other drop is located at $\theta = 0$. The shaded area is the standard deviation. The solid lines are the azimuthal dependencies of the flux for the neighbouring drops normalized by the flux of an isolated drop: $\lim_{r \rightarrow R_0} J_1/J_0$.

a short time after the drop deposition, we can ignore any effect of the contact line motion, as well as the unusual segregation dynamics that occurs in the final phase of evaporation of water/1,2-hexanediol drops (Li *et al.* 2018). Figure 4 (a) shows the trajectories for an isolated drop. The flow is outwards and axisymmetric. There is a stagnation point in the centre of the drop where the particles do not move. Near the rim of the drop, the particles move the most. Some particles are stuck at the contact line.

Figure 4 (b) shows the trajectories for a neighbouring drop (with the neighbouring drop on the left of the drop that is shown). The flow is still outwards, but no longer axisymmetric. The stagnation point has shifted towards the other drop. We also see that the displacement of particles is much larger on the right (away from the other drop) than on the left. The evaporative flux is larger on the right of the drop as the left side is shielded by the other drop. More water evaporates on the right leading to larger concentration gradients in the drop, and consequently larger surface tension gradients. This results in a stronger Marangoni flow, which dominates a larger portion of the drop, shifting the stagnation point towards the other drop.

To better quantify the asymmetry in the velocity in the neighbouring drop, we compute the average velocity of the particles close to the rim for the first 15% of the drop lifetime. We include all the particles in the interval $r/R_0 = [0.8, 0.85]$. When we choose an interval closer to the rim the results become unreliable due to the limited depth of field of the confocal microscope, which brings the flow near the water-vapour interface in focus.

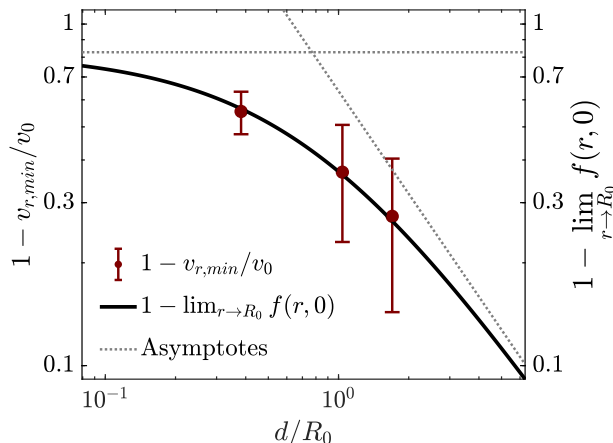


FIGURE 5. The minima in the radial velocity measured between $0.8 < r/R_0 < 0.85$ normalized by the value for an isolated drop, for three different drop separations. The error bar corresponds to the standard deviation. The solid line is the minimum in the local evaporative flux close to the rim, normalized by an isolated drop, as a function of the drop separation (equation 4.3). The asymptotic limits of the flux are shown by the dashed lines: $4/(3\sqrt{3})$ for $d/R_0 \rightarrow 0$, and $2R_0/(\pi d)$ for $d/R_0 \rightarrow \infty$.

Choosing a smaller space and time interval is possible but will result in more noise and a larger statistical error in the data. Figure 4 shows the average radial velocity close to the rim as a function of the azimuthal angle θ in the drop for different drop separations, normalized by the average velocity of an isolated drop. The shaded region corresponds to the standard deviation for each bin.

For $d/R_0 = \infty$ the average velocity is axisymmetric (i.e. constant for all θ). For $d/R_0 = 1.04$, the overall velocity is slightly lower, and a clear minimum appears around $\theta = 0$. For $d/R_0 = 0.38$, the minimum becomes more pronounced, confirming the observations made in figure 4 (b).

Next, we also would like to make a quantitative comparison with the local evaporation rate. To this end we will have to make a few simplifications, since to our knowledge, there is no expression of the local evaporative flux for multi-component drops. However, for single-component drops, the flux has been investigated. [Fabrikant \(1985\)](#) analysed the potential flow through membranes, which is mathematically equivalent to neighbouring evaporating drops. Later, [Wray et al. \(2020\)](#) continued the analysis and calculated the local evaporative flux J_1 of two identical neighbouring drops,

$$J_1(r, \theta) = J_0(r)f(r, \theta). \quad (4.1)$$

Here J_0 is the evaporative flux for an isolated drop,

$$J_0(r) = \frac{2D_{vap}\Delta c_{vap}}{\pi\sqrt{R^2 - r^2}}, \quad (4.2)$$

and $f(r, \theta)$ expresses the shielding effect due to the other drop ([Wray et al. 2020](#)),

$$f(r, \theta) = 1 - \frac{F\sqrt{b^2 - R^2}}{2\pi(r^2 + b^2 - 2rb\cos\theta)}. \quad (4.3)$$

The drop separation is given by b which is the distance from the centres of each drop ($b = d + 2R_0$), where $f(r, \theta)$ is the local shielding, and F is the overall shielding of the

flux, given by $F = 4\pi R/(\pi + 2 \arcsin(R/b))$. Since the flow in the drop is driven by the evaporative flux, we can try to directly compare the measured radial velocity to the result of Wray *et al.* (2020). Even though equations 4.2-4.3 are only valid for single component drops, this can still be a good approximation for the early stages of the evaporation since the drop mostly consists of water with only relatively small concentration differences throughout the drop.

The solid line in figure 4 is the evaporative flux close to the rim for a neighbouring drop, normalized by an isolated drop, i.e. the shielding of the flux by the neighbouring drop: $f(r, \theta)$ evaluated at $r \rightarrow R_0$. Note that no fitting parameters were used. The shape of the curve only depends on the separation between the drops, which was measured using the side view camera.

The agreement between the local flux and the radial velocity is remarkably good. We would like to emphasize that this is not immediately obvious, since the Marangoni flow indirectly depends on the evaporative flux. The shielded evaporative flux in combination with selective evaporation leads to the concentration gradients in the drop. This in turn leads to surface tension gradients which results in Marangoni flow in the drop. It is very reasonable to expect that the flux and radial velocity share *qualitatively* the same shape, but here the agreement is also *quantitative*. This suggests that the relation with the local flux and velocity close to the rim is directly proportional to each other: $J \sim v_r$.

To further quantify the relation between the flux and the radial velocity, we investigate the minimum of J and v_r as shown in figure 4 (c). Figure 5 shows J and v_r at $\theta = 0$ as a function of the drop separation. Despite the large error for the measured radial velocity, the agreement between the velocity and the flux is very good.

5. Conclusion

When two multi-component drops evaporate in close proximity to each other, the shielding effect slows the overall evaporation. Using a confocal microscope with synchronized side view measurements we were able to measure the flow using PTV. We have shown that the flow in the drop becomes asymmetric. The radial velocity close to the rim of the drop is in remarkably good agreement with equation 4.3, the local evaporative flux at the rim for a single component drop.

Additionally, we observed pinning-induced motion of the drops. Based on Marangoni contraction and capillary flow, we would expect the drops to move toward each other, but instead, they move apart. Our hypothesis is that the particles/contaminants in the drop strongly influence the pinning behaviour of the drop. Since the evaporative flux is shielded in the region between the drops, more particles are transported to the part of the drop facing away from the other drop, increasing the likelihood of pinning.

These results are relevant for applications where multiple multi-component drops evaporate simultaneously at close proximity.

Declaration of Interests

The authors report no conflict of interest.

Acknowledgements

This work was supported by an Industrial Partnership Programme, High Tech Systems and Materials (HTSM), of the Netherlands Organisation for Scientific Research

(NWO); a funding for public-private partnerships (PPS) of the Netherlands Enterprise Agency (RVO) and the Ministry of Economic Affairs (EZ); Canon Production Printing Netherlands B.V.; and the University of Twente.

REFERENCES

- BORMASHENKO, E., MUSIN, A. & ZINIGRAD, M. 2011 Evaporation of droplets on strongly and weakly pinning surfaces and dynamics of the triple line. *Colloids and Surfaces A: Physicochemical and Engineering Aspects* **385** (1-3), 235–240.
- BRINKER, C. J., LU, Y., SELINGER, A. & FAN, H. 1999 Evaporation-induced self-assembly: nanostructures made easy. *Advanced Materials* **11** (7), 579–585.
- CHENG, W., ZHANG, W., CHEN, H. & HU, L. 2016 Spray cooling and flash evaporation cooling: The current development and application. *Renewable and Sustainable Energy Reviews* **55**, 614–628.
- CHONG, K.L., LI, Y., NG, C. S., VERZICCO, R. & LOHSE, D. 2020 Convection-dominated dissolution for single and multiple immersed sessile droplets. *Journal of Fluid Mechanics* **892**, A21.
- CIRA, N. J., BENUSIGLIO, A. & PRAKASH, M. 2015 Vapour-mediated sensing and motility in two-component droplets. *Nature* **519** (7544), 446–450.
- DEEGAN, R. D., BAKAJIN, O., DUPONT, T. F., HUBER, G., NAGEL, S. R. & WITTEN, T. A. 1997 Capillary flow as the cause of ring stains from dried liquid drops. *Nature* **389** (6653), 827–829.
- DEEGAN, R. D., BAKAJIN, O., DUPONT, T. F., HUBER, G., NAGEL, S. R. & WITTEN, T. A. 2000 Contact line deposits in an evaporating drop. *Physical Review E* **62** (1), 756.
- DIDDENS, C., LI, Y. & LOHSE, D. 2021 Competing marangoni and rayleigh convection in evaporating binary droplets. *Journal of Fluid Mechanics* **914**, A23.
- DUNN, G. J., WILSON, S. K., DUFFY, B. R., DAVID, S. & SEFIANE, K. 2009 The strong influence of substrate conductivity on droplet evaporation. *Journal of Fluid Mechanics* **623**, 329–351.
- EDWARDS, A. M. J., ATKINSON, P. S., CHEUNG, C. S., LIANG, H., FAIRHURST, D. J. & OUALI, F. F. 2018 Density-driven flows in evaporating binary liquid droplets. *Physical Review Letters* **121** (18), 184501.
- EDWARDS, A. M. J., CATER, J., KILBRIDE, J. J., LE MINTER, P., BROWN, C. V., FAIRHURST, D. J. & OUALI, F. F. 2021 Interferometric measurement of co-operative evaporation in 2d droplet arrays. *Applied Physics Letters* **119** (15).
- FABRIKANT, V. I. 1985 On the potential flow through membranes. *Zeitschrift für angewandte Mathematik und Physik ZAMP* **36** (4), 616–623.
- GELDERBLOM, H., DIDDENS, C. & MARIN, A. 2022 Evaporation-driven liquid flow in sessile droplets. *Soft Matter* **18** (45), 8535–8553.
- GIMENES, M. J., ZHU, H., RAETANO, C. G. & OLIVEIRA, R. B. 2013 Dispersion and evaporation of droplets amended with adjuvants on soybeans. *Crop Protection* **44**, 84–90.
- HACK, M. A., KWIECINSKI, W., RAMÍREZ-SOTO, O., SEGERS, T., KARPITSCHKA, S., KOOLJ, E. S. & SNOEIJER, J. H. 2021 Wetting of two-component drops: Marangoni contraction versus autophobing. *Langmuir* **37** (12), 3605–3611.
- HATTE, S., PANDEY, K., PANDEY, K., CHAKRABORTY, S. & BASU, S. 2019 Universal evaporation dynamics of ordered arrays of sessile droplets. *Journal of Fluid Mechanics* **866**, 61–81.
- HOATH, S. D. 2016 *Fundamentals of inkjet printing: the science of inkjet and droplets*. John Wiley & Sons.
- KANT, P., SOUZY, M., KIM, N., VAN DER MEER, D. & LOHSE, D. 2024 Autothermotaxis of volatile drops. *Physical Review Fluids* **9** (1), L012001.
- KARPITSCHKA, S., LIEBIG, F. & RIEGLER, H. 2017 Marangoni contraction of evaporating sessile droplets of binary mixtures. *Langmuir* **33** (19), 4682–4687.
- KHILIFI, D., FOU DHIL, W., FAHEM, K., HARMAND, S. & BEN, J. S. 2019 Study of the phenomenon of the interaction between sessile drops during evaporation. *Thermal Science* **23** (2 Part B), 1105–1114.

- LAGHEZZA, G., DIETRICH, E., YEOMANS, J. M., LEDESMA-AGUILAR, R., KOUIJ, E. S., ZANDVLIET, H. J. W. & LOHSE, D. 2016 Collective and convective effects compete in patterns of dissolving surface droplets. *Soft Matter* **12** (26), 5787–5796.
- LARSON, R. G. 2014 Transport and deposition patterns in drying sessile droplets. *AIChE Journal* **60** (5), 1538–1571.
- LI, Y., LV, P., DIDDENS, C., TAN, H., WIJSHOFF, H., VERSLUIS, M. & LOHSE, D. 2018 Evaporation-triggered segregation of sessile binary droplets. *Physical Review Letters* **120** (22), 224501.
- LOHSE, D. 2022 Fundamental fluid dynamics challenges in inkjet printing. *Annual Review of Fluid Mechanics* **54**, 349–382.
- MAMPALLIL, D. & ERAL, H. B. 2018 A review on suppression and utilization of the coffee-ring effect. *Advances in colloid and interface science* **252**, 38–54.
- MASOUD, H., HOWELL, P. D. & STONE, H. A. 2021 Evaporation of multiple droplets. *Journal of Fluid Mechanics* **927**, R4.
- NGUYEN, T. A. H., NGUYEN, A. V., HAMPTON, M. A., XU, Z. P., HUANG, L. & RUDOLPH, V. 2012 Theoretical and experimental analysis of droplet evaporation on solid surfaces. *Chemical Engineering Science* **69** (1), 522–529.
- PAHLAVAN, A. A., YANG, L., BAIN, C. D. & STONE, H. A. 2021 Evaporation of binary-mixture liquid droplets: the formation of picoliter pancakelike shapes. *Physical Review Letters* **127** (2), 024501.
- SCHOFIELD, F. G. H., WRAY, A. W., PRITCHARD, D. & WILSON, S. K. 2020 The shielding effect extends the lifetimes of two-dimensional sessile droplets. *Journal of Engineering Mathematics* **120** (1), 89–110.
- SHIRI, S., SINHA, S., BAUMGARTNER, D. A. & CIRA, N. J. 2021 Thermal marangoni flow impacts the shape of single component volatile droplets on thin, completely wetting substrates. *Physical Review Letters* **127** (2), 024502.
- STAUBER, J. M., WILSON, S. K., DUFFY, B. R. & SEFIANE, K. 2014 On the lifetimes of evaporating droplets. *Journal of Fluid Mechanics* **744**, R2.
- STAUBER, J. M., WILSON, S. K., DUFFY, B. R. & SEFIANE, K. 2015 On the lifetimes of evaporating droplets with related initial and receding contact angles. *Physics of fluids* **27** (12).
- THAYYIL RAJU, L., DIDDENS, C., LI, Y., MARIN, A., VAN DER LINDEN, M. N., ZHANG, X. & LOHSE, D. 2022 Evaporation of a sessile colloidal water–glycerol droplet: Marangoni ring formation. *Langmuir* **38** (39), 12082–12094.
- WANG, Z., OREJON, D., TAKATA, Y. & SEFIANE, K. 2022 Wetting and evaporation of multicomponent droplets. *Physics Reports* **960**, 1–37.
- WIJSHOFF, H. 2018 Drop dynamics in the inkjet printing process. *Current Opinion in Colloid & Interface Science* **36**, 20–27.
- WILSON, S. K. & D’AMBROSIO, H. 2023 Evaporation of sessile droplets. *Annual Review of Fluid Mechanics* **55**, 481–509.
- WRAY, A. W., DUFFY, B. R. & WILSON, S. K. 2020 Competitive evaporation of multiple sessile droplets. *Journal of Fluid Mechanics* **884**, A45.
- WRAY, A. W., WRAY, P. S., DUFFY, B. R. & WILSON, S. K. 2021 Contact-line deposits from multiple evaporating droplets. *Physical Review Fluids* **6** (7), 073604.
- YU, Y., ZHU, H., FRANTZ, J. M., REDING, M. E., CHAN, K. C. & OZKAN, H. E. 2009 Evaporation and coverage area of pesticide droplets on hairy and waxy leaves. *Biosyst. Eng.* **104** (3), 324–334.
- ZANG, D., TARAFDAR, S., TARASEVICH, Y. Y., CHOUDHURY, M. D. & DUTTA, T. 2019 Evaporation of a droplet: From physics to applications. *Physics Reports* **804**, 1–56.

Supplementary information for: ‘Pinning induced motion and internal flow in neighbouring evaporating multi-component drops’

Pim J. Dekker

*Physics of Fluids group, Department of Science and Technology,
Max Planck Center for Complex Fluid Dynamics and J. M. Burgers Centre for Fluid Dynamics,
University of Twente, P.O. Box 217, 7500 AE Enschede, The Netherlands*

Marjolein N. van der Linden

*Canon Production Printing Netherlands B.V., P.O. Box 101, 5900 MA Venlo, The Netherlands and
Physics of Fluids group, Department of Science and Technology,
Max Planck Center for Complex Fluid Dynamics and J. M. Burgers Centre for Fluid Dynamics,
University of Twente, P.O. Box 217, 7500 AE Enschede, The Netherlands*

Detlef Lohse

*Physics of Fluids group, Department of Science and Technology,
Max Planck Center for Complex Fluid Dynamics and J. M. Burgers Centre for Fluid Dynamics,
University of Twente, P.O. Box 217, 7500 AE Enschede, The Netherlands and
Max Planck Institute for Dynamics and Self-Organization, Am Fassberg 17, 37077 Göttingen, Germany
(Dated: December 12, 2024)*

This Supplementary Information presents details regarding the experimental setup, procedures, and processing of the captured images and data. Additionally, we confirm that the evaporation is well described by the diffusion limited evaporation model.

SETUP

Fig. 1 shows a schematic of the confocal microscope used for the measurements. To ensure that the experiments are repeatable and reproducible we had to monitor and control the ambient humidity and temperature in which the drop evaporates. To achieve this, we made a transparent acrylic chamber that fits inside the translation stage of the confocal. A schematic of the humidity chamber is shown in Fig. 2. To not interfere with the optics of the confocal microscope, there is no acrylic directly below the glass substrate. Unfortunately, this means that the chamber is not perfectly air-tight, and that the humidity will very slowly drift towards the ambient humidity in the lab. Additionally, at the start of each experiment the drops are deposited through a small door temporarily allowing some air in and out the chamber. Therefore, we have strived to keep the humidity in the chamber close to the humidity in the lab when doing experiments.

The humidity is controlled using an in-house humidity controller, for which the schematics and codes are publicly available on GitHub (<https://github.com/Dennis-van-Gils/project-Humidistat>). We monitor the humidity in the chamber with a digital sensor (Bosch Sensortec BME280) that measures humidity, temperature, and pressure. There are two sensors in the humidity chamber, one is very close to the substrate with the drop (1-2 cm) whereas the other sensor is as far away as possible from the drop (7-8 cm) in the upper corner of the humidity chamber. This allows us to assess the absolute and relative accuracy of the sensors, as well as the homogeneity of the relative humidity in the chamber. The sensors are connected to a microcontroller (Adafruit Feather M4 Express) which controls two solenoid valves. One is connected directly to the compressed nitrogen that is available in the lab (resulting in very dry air), the other passes first through a porous stone submerged in water (resulting in very humid air). Using this setup, we can achieve relative humidities between 25% and 85%. During every experiment, both solenoid valves were closed to prevent any airflow in the chamber.

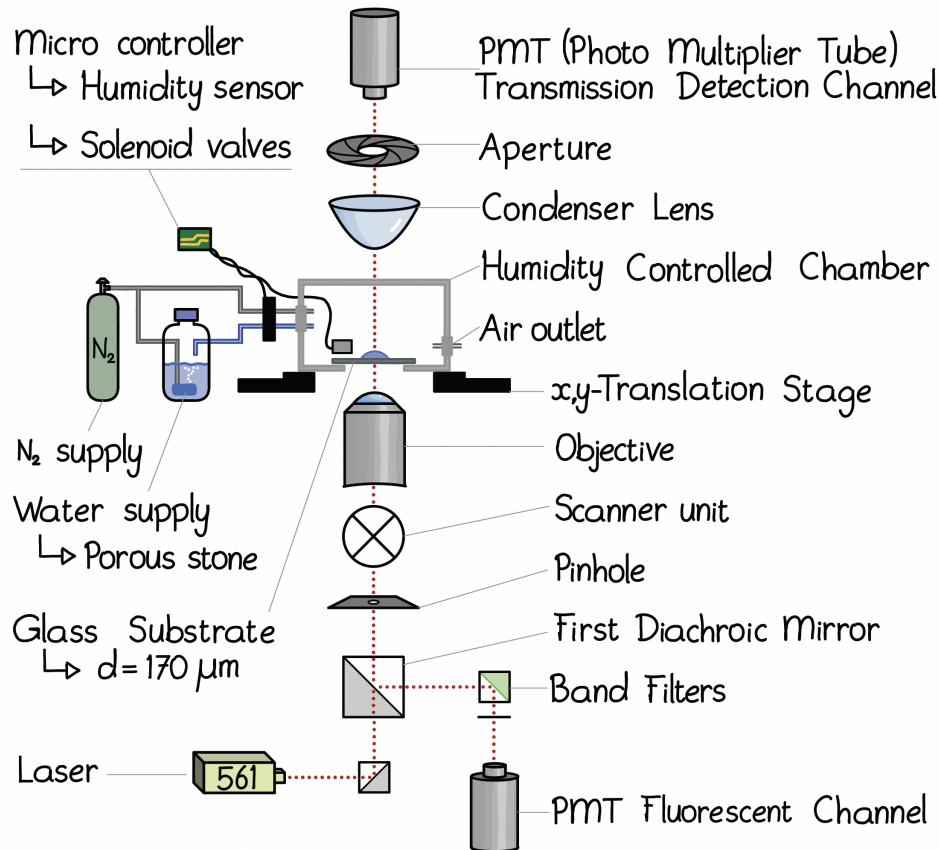


FIG. 1. Schematic of the setup.

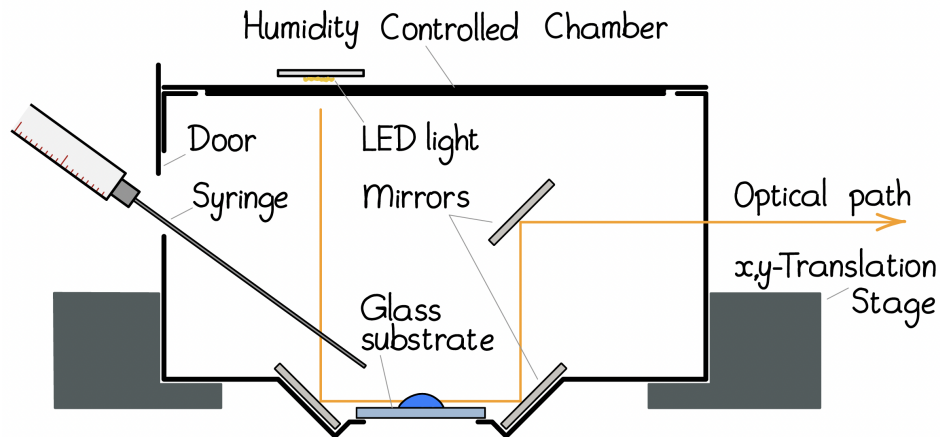


FIG. 2. Schematic of the humidity chamber. (Not to scale)

The side view of the drop poses an extra challenge due to the requirements of the confocal and the humidity chamber. Namely, the substrate must be sufficiently close to the microscope objective to obtain an image. That means it is not possible to image the drop from the side directly because the view is obstructed by the translation stage (see Fig. Fig. 2). To solve this problem, we placed mirrors inside the chamber. However, this significantly increased the optical path length from the lens to the drop. This required a long-distance microscope lens with a sufficiently long working distance to be able to see the drop. The lens that we used is a modular Navitar lens with the following components: 2× F-Mount (1-62922), 12× Zoom (1-50486), 0.5× Lens Attachment (1-50012), Right Angle Lens Attachment (1-51490). This lens has a sufficiently large working distance of 165 mm, a maximum magnification of 7× and a resolve limit of 6.66 μm .

SIDE VIEW MEASUREMENTS

The side view allows us to track the positions of the drop and to measure the drop volume over time. Fig. 3(a) shows a typical image captured by the side view camera. Although the drop appears tilted, the substrate is perfectly level. The tilt is introduced due to the imperfect alignment of the mirrors. The side view is pitched 4° forward such that the reflection of the drop is visible in the substrate.

Before processing the image, the intensities of the captured image are normalized between 0 and 1. Then we apply a Gaussian blur with standard deviation $\sigma = 2$ px. This reduces the noise in the image significantly without compromising the information of the drop interface, since the features of the drop are much larger than the applied blur. The system is lens limited since the resolution of the camera is 0.64 $\mu\text{m}/\text{px}$, which makes one pixel approximately 10 times smaller than the optical resolution of the lens. We distinguish the drop from the background by binarizing the image using a threshold of 0.5. Using morphological operations we fill any speckles/reflections in the drop interior and the background. To identify the edge, we calculate intersection between the threshold and the intensities to obtain the interface with sub-pixel accuracy. We do this for every column of pixels in the image, such that we can easily differentiate between the top and bottom interface.

Next, we fit a circle to the top and bottom interface using the least squares method. This fit returns the radii (r_1, r_2) and the centers of the top and bottom circle respectively (x_1, y_1 and x_2, x_2). Using geometry (Fig. 4) we can calculate the tilt of the camera, the contact angle of the drop, and the contact radius of the drop. The volume of a spherical cap is given by the following:

$$V = \frac{\pi R^3}{6} (2 + \cos \theta) \frac{\sin(\theta/2)}{\cos^3(\theta/2)} \quad (1)$$

The results of the volume, contact radius, and contact angle for an isolated are shown in Fig. 5. Additionally the relative humidity and the temperature measured by the near- and far-away sensor are shown. As the drop is deposited, the sensors show a sharp increase in the humidity. The sensor close to the drop increases much more sharply than

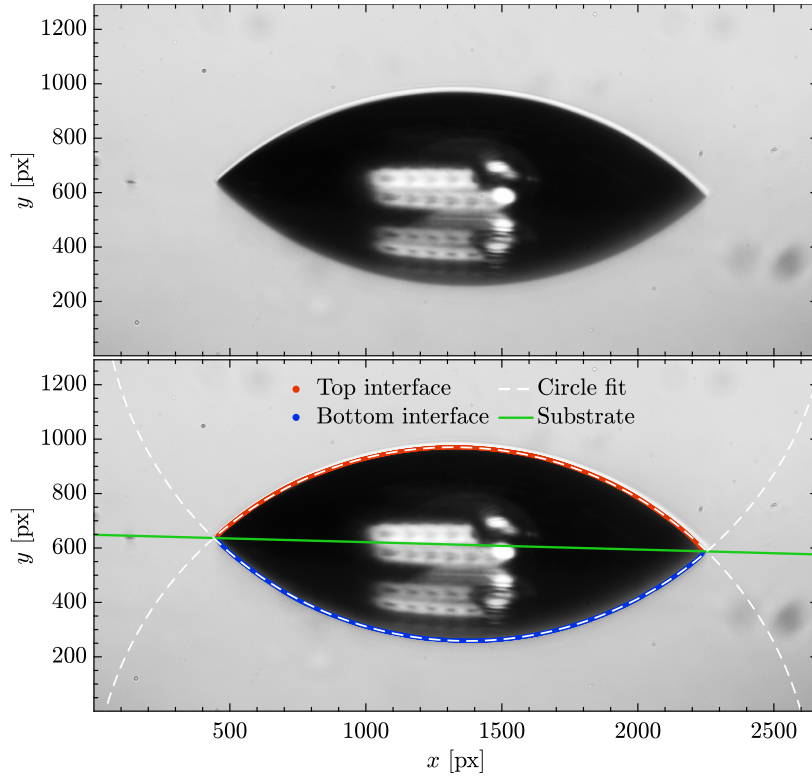


FIG. 3. Top panel: Image captured by the side view camera. Bottom panel: Detected interface and the fitted circle of the side view image.

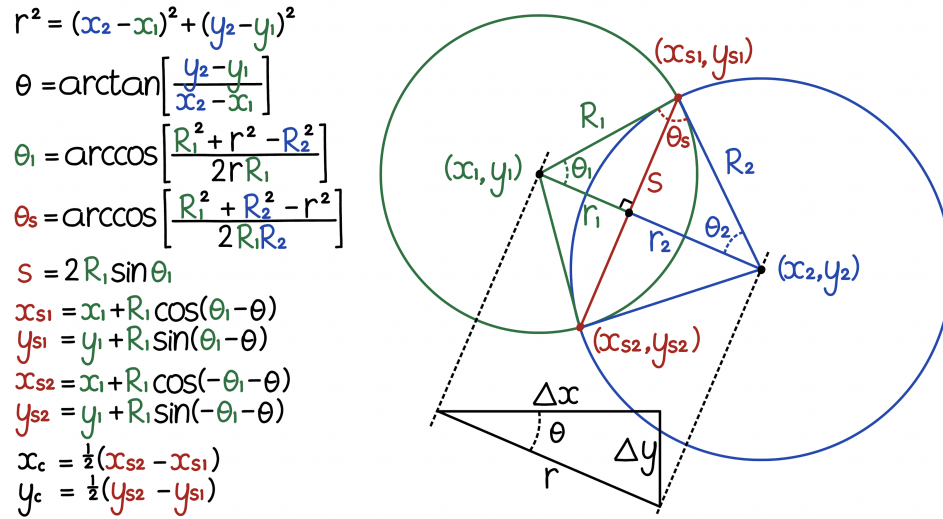


FIG. 4. Geometry of two intersecting circles.

the sensor far from the drop. When the drop has evaporated, the humidity measured by the sensor close to the drop decreases, but the sensor far from the drop remains unaffected. This indicates that the chamber sufficiently large to be considered an infinite medium.

To further validate that the evaporation is indeed diffusion limited, we have also calculated and compared the volume evolution with the diffusion limited evaporation model (Popov, 2005). In this model it is assumed that the transport mechanism that governs the evaporation speed is the diffusion of water vapour through the air and the

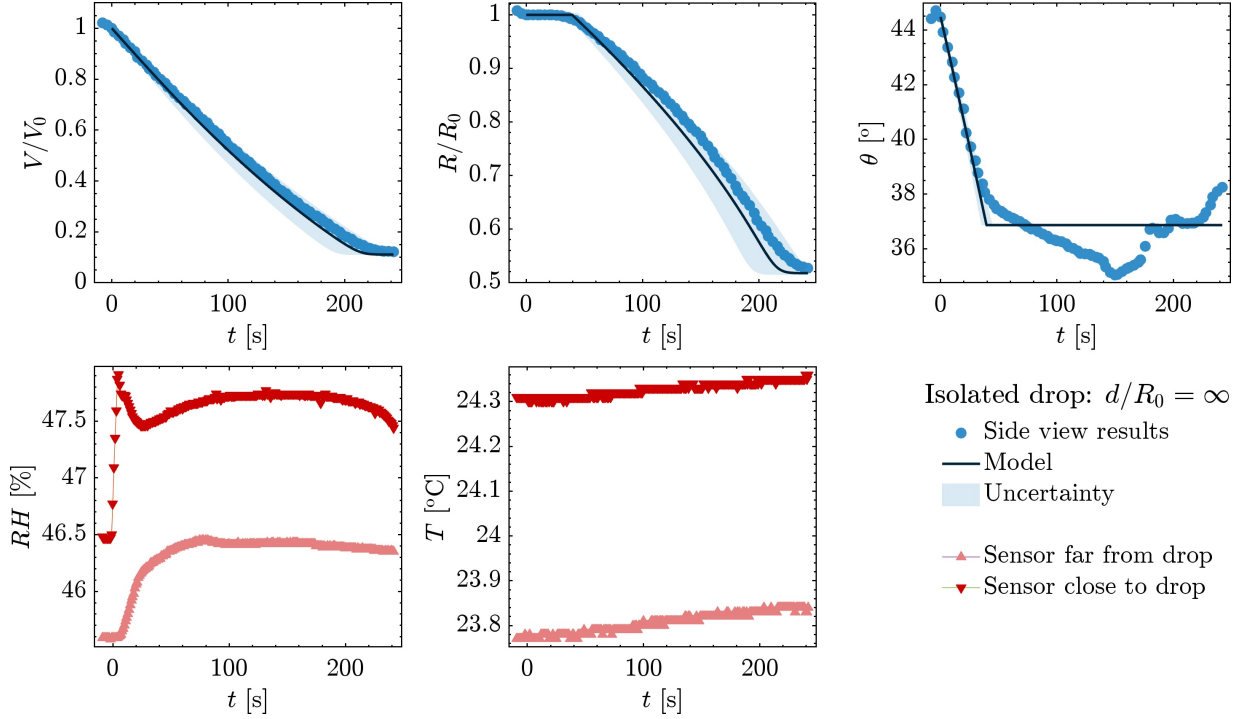


FIG. 5. Isolated drop with initial 1,2-hexanediol concentration of 10 wt%. Top row: evolution of the drop volume, contact radius, and contact angle during evaporation. The solid lines are calculated using the diffusion limited evaporation model where the initial conditions are based on the measurements. The shaded region is the variation in the model due to the uncertainty in the measured quantities. Bottom row: the measured humidity and temperature for the nearby sensor and the far-away sensor. Initial conditions: $V_0 = 0.135 \pm 0.002 \mu\text{l}$, $R_0 = 0.583 \pm 0.002 \text{ mm}$.

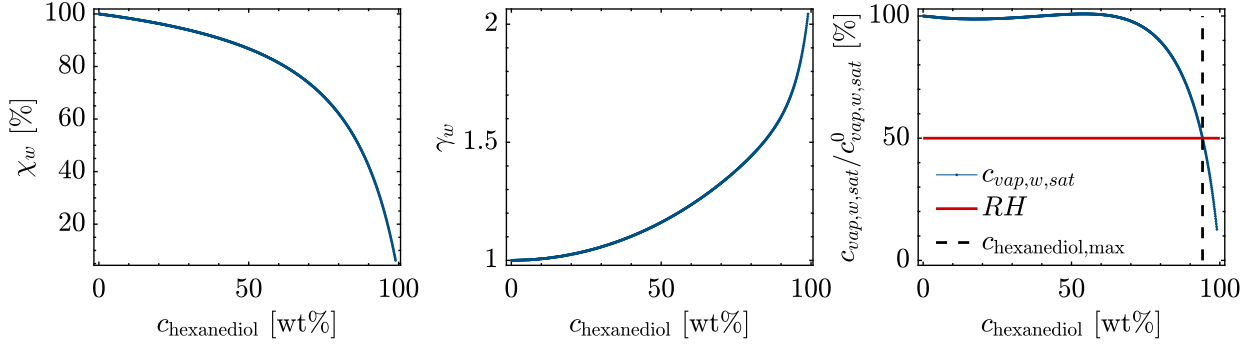


FIG. 6. Left panel: *mole* fraction of water versus the *mass* fraction of hexanediol. Center panel: Activity coefficient of water versus the mass fraction of hexanediol. Right panel: normalized saturated vapour concentration of water versus the mass fraction of hexanediol. Up to $C_{\text{hexanediol}} = 70 \text{ wt}\%$ the evaporation speed will remain close to that of pure water since $c_{\text{vap},w,\text{sat}}/c_{\text{vap},w,\text{sat}}^0 > 98\%$. For a relative humidity of 50% the evaporation will cease at 94 wt% hexanediol, as is indicated by the dashed line.

mass flux is given by

$$\frac{dm}{dt} = -\pi R D_{\text{vap},w} \Delta c_{\text{vap},w} g(\theta). \quad (2)$$

Here, $D_{\text{vap},w}$ is the diffusion coefficient of water vapour in air, $\Delta c_{\text{vap},w}$ the water vapour concentration difference, and $g(\theta)$ is a geometric factor that depends only on the contact angle and is given by

$$g(\theta) = \frac{\sin \theta}{1 + \cos \theta} + 4 \int_0^\infty \frac{1 + \cosh 2\theta\tau}{\sinh 2\pi\tau} \tanh [(\pi - \theta)\tau] d\tau. \quad (3)$$

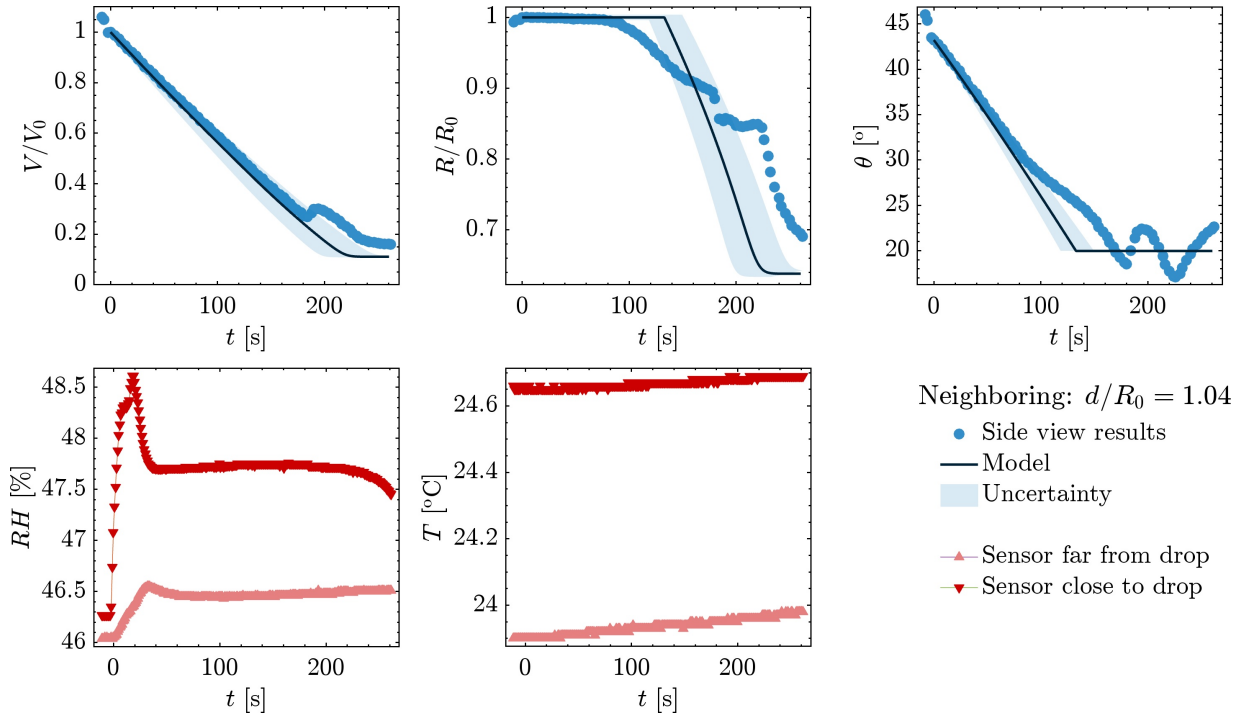


FIG. 7. neighbouring drop with initial 1,2-hexanediol concentration of 10 wt%. Top row: evolution of the drop volume, contact radius, and contact angle during evaporation. The solid lines are calculated using the diffusion limited evaporation model where the initial conditions are based on the measurements. The shaded region is the variation in the model due to the uncertainty in the measured quantities. Bottom row: the measured humidity and temperature for the nearby sensor and the far-away sensor. Initial conditions: $V_0 = 0.124 \pm 0.002 \mu\text{l}$, $R_0 = 0.573 \pm 0.003 \text{ mm}$.

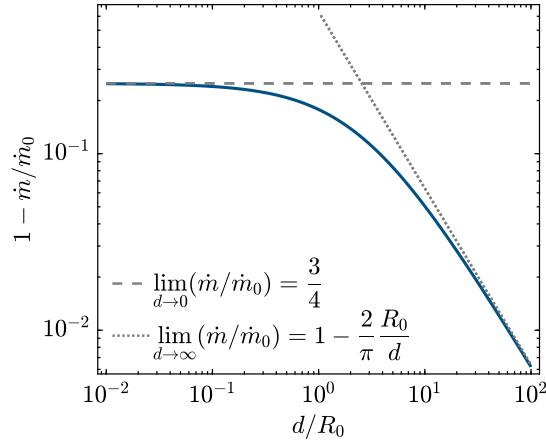


FIG. 8. Reduction in the total mass flux due to the shielding effect of an identical neighbouring drop with initial contact radius R_0 at distance d . In the limit of touching drops ($d \ll R_0$), both drops evaporate 25% slower. When the distance between the drops is large ($d \gg R_0$), the shielding effect of the neighbouring drop diminishes as d^{-1} .

The evaporation speed is directly proportional to the concentration difference in water vapour at the drop surface and at infinity. For a pure drop this is given by

$$\Delta c_{vap,w}^0 = c_{vap,w,sat}^0 (1 - RH). \quad (4)$$

Here, $c_{vap,w,sat}^0$ is the saturated vapour concentration of pure water, and RH the relative humidity. However, for a binary mixture the saturated vapour concentration depends on the concentration of the other species according to

Raoult's law. For a binary mixture the concentration difference is given by

$$\Delta c_{vap,w} = c_{vap,w,sat}^0 (\chi_w \gamma_w - RH). \quad (5)$$

Here, χ_w is the mole fraction of water in the drop at the surface, and γ_w the activity coefficient which takes the non-ideal interactions into account. γ_w can be estimated using models such as the AIOMFAC model (Zuend et al., 2008) (<https://aiomfac.lab.mcgill.ca/index.html>). When $\chi_w \gamma_w = RH$ the evaporation will cease, meaning that for a non-zero relative humidity not all water will evaporate as is further illustrated in Fig. 6. Note that we only have to consider the evaporation of water, since hexanediol is non-volatile. Additionally, we have assumed that the drop is well mixed at all times. A similar adaptation of the diffusion limited model has been used before to successfully describe the evaporation of a binary drop of water and glycerol (Raju et al., 2022).

Now we still need to identify the contact line behavior of the drop to fully describe the evaporation. Initially, the drop is pinned and evaporates in constant contact radius mode (CCR). When the contact angle reaches 38° the drop continues in constant contact angle mode (CCA). However, the contact angle isn't perfectly constant. A possible explanation is that the changing composition due to evaporation leads to a different equilibrium contact angle. In our model we reflect the contact line behavior by starting in CCR mode until a critical contact angle of $\theta_c = 37^\circ$ after which the drop continues in CCA mode.

The solid line in Fig. 5 is the result of the model with the same initial conditions as measured in the experiment. The shaded region corresponds to the variation in outcome of the model due to the uncertainty in the measured experimental values. Qualitatively, the model agrees very well with the measured volume. Quantitatively, the model predicts a slightly faster evaporation speed. However, we did not consider the effect of evaporative cooling on the evaporation speed. After approximately 240 s the evaporation ceases and the measured volume is 12.2% of the initial volume. The volume predicted by the model is at 11.1% of the initial volume. In the model we assumed that the drop is always well mixed. This assumption breaks down at the end of the drop life time as the diffusion of water through the liquid hexanediol becomes the limiting mechanism of evaporation.

Fig. 7 shows the volume evolution for a neighbouring evaporating drop. In order to apply the diffusion limited model we need to consider the shielding effect of the neighbouring drop. For two identical pure drops with initial contact radius R_0 and separated by distance d in the limit of $\theta \rightarrow 0$ and $d/R_0 \rightarrow \infty$ the integral shielding factor F is given by (Fabrikant, 1985; Wray et al., 2020)

$$F = \frac{\dot{m}}{\dot{m}_0} = \frac{1}{1 + \frac{2}{\pi} \arcsin\left(\frac{R}{d + 2R_0}\right)}. \quad (6)$$

Here, \dot{m}_0 is the mass flux for an isolated drop and \dot{m} is the mass flux for a neighbouring drop. Fig. 8 show the shielding factor as a function of drop separation. Comparing the model with the experiment we find good agreement. Note that the apparent increase in volume at $t = 200$ s is due to the contact line behavior where the drop shape temporarily deviates from a spherical cap.

By applying Raoult's law and the shielding factor we can predict the volume evolution of evaporating neighbouring binary drop very well using the diffusion limited evaporation model. The volume loss rate predicted by the model is consistently slightly larger since we did not consider evaporative cooling.

PARTICLE TRACKING VELOCIMETRY (PTV)

The defining feature of the confocal is its very narrow depth of field (DoF). By focusing at the substrate we can observe and follow small fluorescent particles that are carried with the flow, allowing us to visualize and quantify the flow. In this section we will describe the method and processing that we used to obtain quantitative information of the flow in the drop.

The confocal settings were as follows: Objective: magnification = $10\times$; $NA = 0.3$; optical resolution: $1.03\ \mu\text{m}$. The scan area was 512 by 512 pixels, resulting in a pixel size of $2.50\ \mu\text{m}$, and a field of view of $1.28\ \text{mm}$. The confocal scan mode was set to resonant mode. To increase the signal to noise ratio, we average every line 4 times, resulting in 7.7 frames per second. The pinhole size was: $29.4\ \mu\text{m}$. Laser wavelength = $561\ \text{nm}$, detection range: $570\ \text{nm} - 620\ \text{nm}$.

To estimate the effective DoF (depth of field) of the confocal microscope we scanned a single fluorescent particle at different heights. Fig. 9 shows the slices of the particle in different planes. We can observe that the particle appears to be much larger in the y -plane as compared to the x -plane, this is an optical artifact of the scanning mode of the confocal. We see beyond $z = 20\ \mu\text{m}$ that the particle almost completely faded and we only measure some noise.

Particle detection

Fig. 10(a.i) shows an image captured by the confocal. Before processing, the intensities are normalized between 0 and 1 . To detect the particle positions we apply a threshold of 0.45 resulting in a binary image as shown in Fig. 10(b). Each region of connected white pixels corresponds to a particle. To accurately determine the position of the particle we use the intensity of the original image, not the binarized image. First, we expand the region to include by 1 pixel, such that we do not miss neighbouring pixels that are just below the threshold but still relevant to the particle position. Fig. 10(b.iii) shows the expanded particle region with the green line.

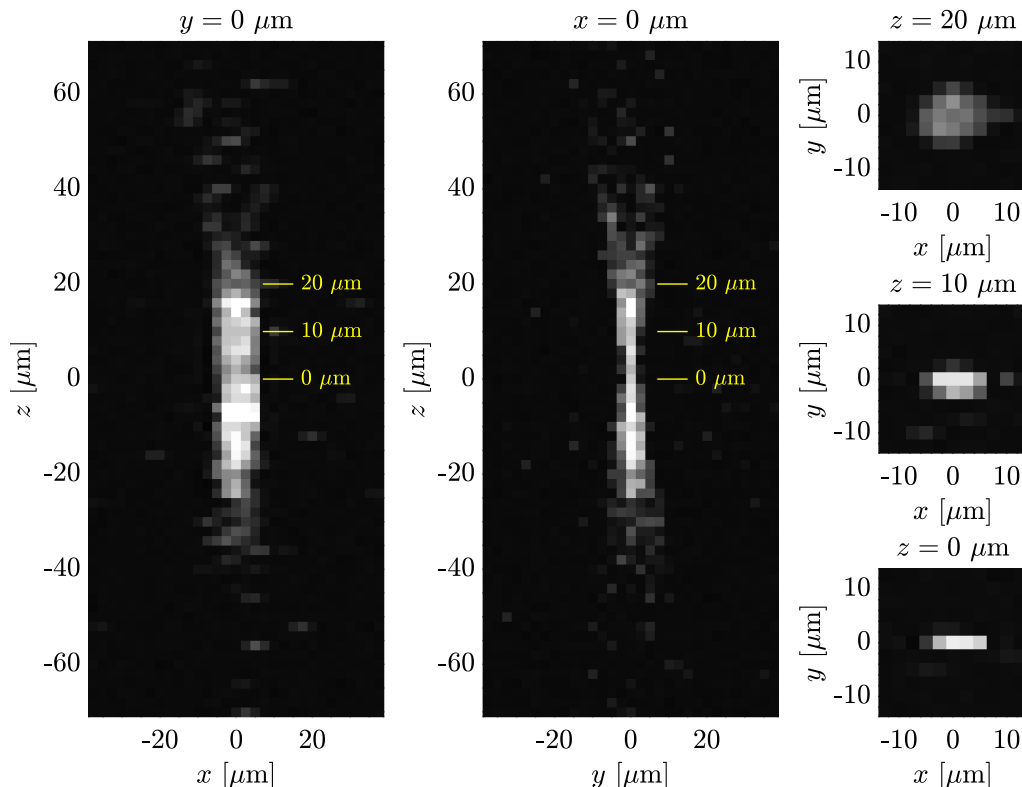


FIG. 9. Depth of field of the confocal microscope at $10\times$ magnification and $NA = 0.3$ and fluorescent particles with a diameter of $d = 1.14\ \mu\text{m}$. Slices in different directions are shown of a single particle.

Next, the particle position (p_x, p_y) is determined by calculating the ‘center of intensity’ region (analogous to the ‘center of mass’) for each pixel. This is given by the following relations

$$p_x = \frac{\sum x_i I(x_i, y_i)}{\sum I(x_i, y_i)}, \quad (7)$$

$$p_y = \frac{\sum y_i I(x_i, y_i)}{\sum I(x_i, y_i)}. \quad (8)$$

Here, we sum over all the pixels in the particle region. The resulting particle positions are shown in Fig. 10(c). Note that this method can detect a displacement much smaller than a single pixel. Additionally, by using the intensities in

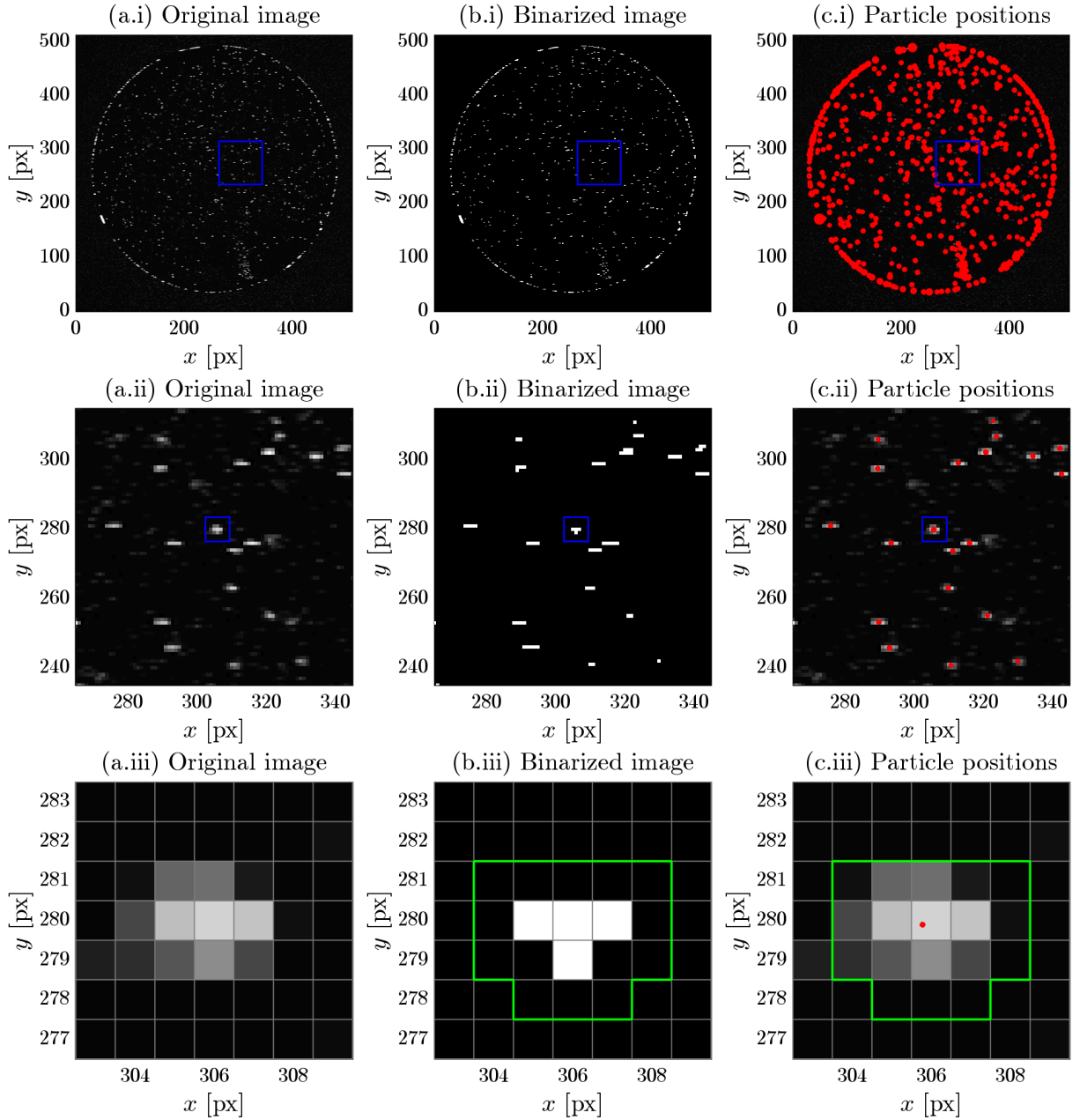


FIG. 10. Particle detection. Columns: (a) original image as captured by the confocal; (b) image binarized using threshold; (c) original image with the detected particle positions. Rows: (i) full image; (ii) center of the image; (iii) single particle. The zoomed-in sections are highlighted with a blue box. The green line (b.iii) and (c.iii) indicates the region used to calculate the particle position and particle size.

the original image we can determine the particle positions much more accurately as compared to the binary image, which contains far less information.

Finally, we filter out particles that are incorrectly detected as particles. We do this based on the size of the particles, which we calculate using,

$$p_{size} = \frac{\sum I(x_i, y_i)}{I_0}. \quad (9)$$

This is simply the sum of all the intensities of the pixels in the particle region. This is very similar to a ‘particle mass’. Note that this is *not* a particle radius. When a particle size is very small, it is much more likely to be noise. When a particle size is very large, it is likely a cluster of multiple particles that are very close or even overlapping. Fig. 11 shows the probability density function of the particle size distribution. All particles smaller than 1.25 or larger than 10 are excluded.

Particle matching

Now that we have the particle positions for each frame, we need to match the detected particles between the different frames to reconstruct their trajectories. Since the displacement of the particles between consecutive frames is very little, we can use the nearest-neighbor approach. For each particle in frame n we calculate the distance to all the other particles in frame $n + 1$. We then match the particle with the smallest distance.

To prevent mismatches, we apply the following criteria.

- If the distance between the particles is 5 pixels or larger, it is very likely to match the wrong particle.
- If multiple particles are found within a 1-pixel radius, we cannot distinguish the particles well enough to match them with certainty.
- If a particle in frame $n + 1$ has been matched to multiple particles in frame n , we also disregard those matches.

The small displacement of particles between frames makes the matching process computationally very straightforward. With the above criteria we lose some information when multiple particles are in close proximity, although more advanced methods can distinguish overlapping particles, with the current method we retain a sufficient amount of information for analysis. For all successfully matched particle trajectories we require that the minimum trajectory length is at least 15 frames. Due to the large frame rate we need this many frames to obtain any relevant displacement to ensure accurate velocity measurements.

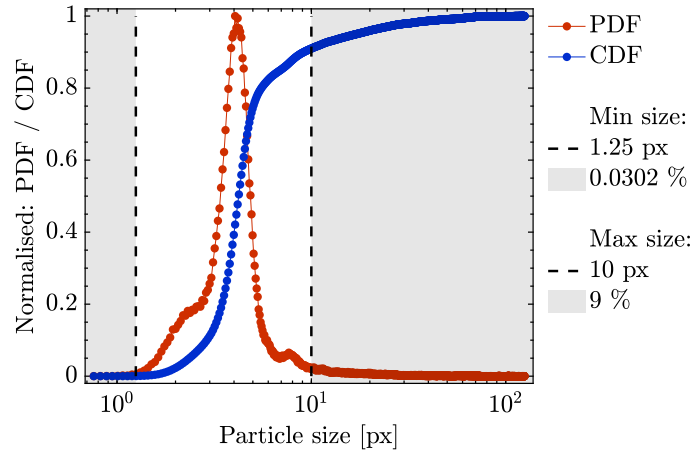


FIG. 11. Probability density function (PDF) and cumulative probability density function (CDF) of the particle sizes (sum of the intensities). The regions highlighted in gray are limiting particle sizes below and above which are omitted. The percentage of eliminated particles is shown in the legend.

Due to noise in the image and naturally present Brownian motion of the particles, the velocities that we measure are very noisy. To eliminate some of the noise without compromising the signal we apply a filter, which is a moving average with the following kernel: $[1/4, 1/2, 1/4]$. This filter is applied to both the positions of the particles before calculating the particle velocities, as well as after calculating the particle velocity. Note that the filtering we apply is minimal and that after filtering the data is still very noisy. This is a deliberate choice, since we will bin and average the data later. Keeping the noise allows us to quantify the noise/Brownian motion of the particles.

Azimuthal dependence of the radial velocity

Now that we have calculated all the trajectories and velocities of all the particles in the drop we can extract the azimuthal dependence of the radial velocity close to the contact line for all the measurements. Fig. 12(a.i) shows all measured radial velocities versus the radial position for an isolated drop. Close to $r/R_0 = 0$ the velocities are below $0.5 \mu\text{m/s}$ which is likely Brownian motion. As we approach the contact line (i.e. $r/R_0 = 1$), the measured radial velocities start to increase. After $r/R_0 = 0.6$ we see two branches of radial velocities. One velocity-branch continues to increase approaching the contact line. However, the other velocity-branch remains close to $v_r = 0$.

Next we take all the radial velocities that we measured between 0.8 and 0.85 and plot those velocities as a function of the azimuthal position in the drop as shown in Fig. 12(a.ii). Here we can observe again a split in the measured velocities, there are a large number of measurements around $v_r = 2 \mu\text{m/s}$ and concentrated patches of measurements at $v_r = 0 \mu\text{m/s}$. Our interpretation is that some particles are strongly interacting with the substrate and are no longer acting as reliable tracer particles. Whereas other particles, which are slightly further away from the substrate, are still valid tracer particles. Unfortunately, the particles which are slow/stuck have a large impact on the average radial velocity since they are always between $0.8 < r/R_0 < 0.85$. In contrast, the particles following the flow are only briefly in the same window.

To be able to distinguish between the slow/stuck particles and the valid tracer particles, we discriminate between them using a "Brownian speed limit". Using the Stokes–Einstein equation we can compute the diffusivity D_p of a particle with radius r_p subject to Brownian motion in a liquid with viscosity μ with

$$D_p = \frac{k_b T}{6\pi\mu r_p}. \quad (10)$$

Here, k_b is the Boltzmann constant and T the absolute temperature. With the diffusion coefficient we can estimate how far the particles will travel between two consecutive frames recorded by the confocal and use this to compute the perceived velocity of the particles due to Brownian motion with

$$v_{Brown} = \sqrt{\frac{D_p}{N_{ave}\tau_{frame}}} \approx 0.7 \mu\text{m/s}. \quad (11)$$

Here, N_{ave} takes the filtering of the velocities into account, and τ_{frame} is the time between two recorded frames.

Fig. 12(b.ii) shows the result when we apply this speed limit of $0.7 \mu\text{m/s}$ on the azimuthal distribution of the radial velocity. The sharp spikes are now filtered out. Fig. 12(c) and (d) show the radial velocities for neighbouring drops. Both suffer from the same problem of slow/stuck particles near the substrate. Note that without applying the "speed limit" the data becomes a lot more noisier, but the results and conclusions in the main text remain the same.

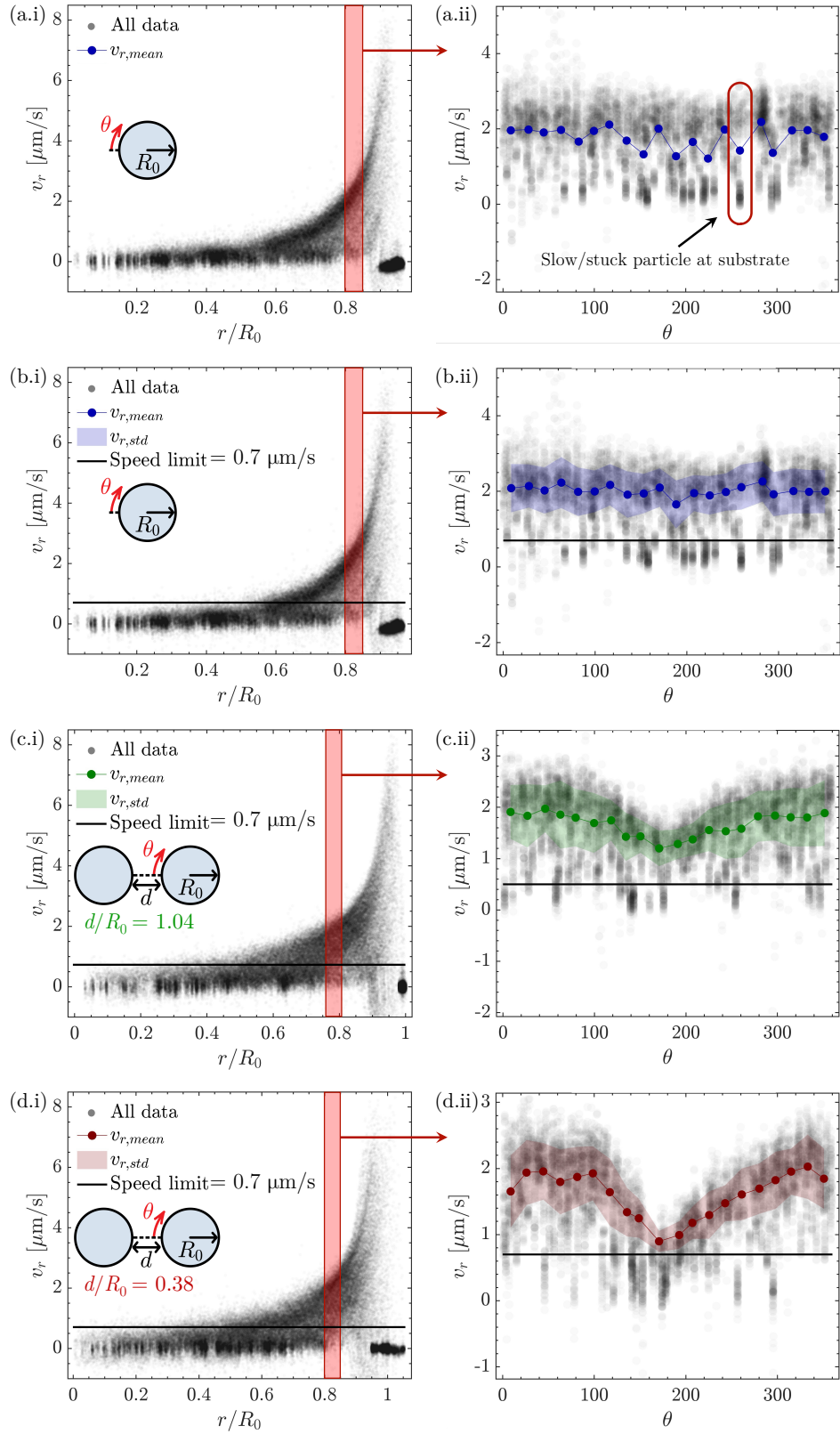


FIG. 12. Radial velocity measurements using PTV. Column (i): All radial velocities v_r versus the radial position r/R_0 in the drop. Column (ii): Radial velocities v_r on the interval $0.8 < r/R_0 < 0.85$ versus the azimuthal position θ in the drop. Row (a): Isolated drop *without* velocity limit. Row (b): Isolated drop *with* velocity limit. Row (c): neighbouring drop at distance $d/R_0 = 1.04$. Row (d): neighbouring drop at distance $d/R_0 = 0.38$